Nonlinear Beam Shaping with Binary Phase Modulation on Patterned WS$_2$ Monolayer

Arindam Dasgupta, Xiaodong Yang,* and Jie Gao*

Cite This: *ACS Photonics* 2020, 7, 2506−2514

Read Online

ACCESS | Metrics & More | Article Recommendations

ABSTRACT: The capability of controlling the phase of the nonlinear polarization of media is vital for nonlinear optical beam shaping. Achieving this control over nonlinear phase manipulation on the nanoscale facilitates modern on-chip photonic integration of nonlinear beam shaping. Plasmonic metasurfaces with thickness down to tens of nanometers can be used to provide the continuous local phases of the nonlinear polarization via the spin-rotation coupling of light, but they still suffer from low conversion efficiency and high absorption loss. Concomitantly, the thickness of dielectric metasurfaces cannot be brought down to a scale lower than hundreds of nanometers. In that context, transition metal dichalcogenide (TMD) monolayers with atomic thickness are known to have high nonlinear conversion efficiency. With that hindsight, here we explain how to manipulate the local phase of the nonlinear polarization from the rotated WS$_2$ monolayer crystals. To verify the theoretical prediction, we also experimentally demonstrate the nonlinear generation of Hermite−Gaussian beams at second-harmonic frequencies via the binary phase manipulation on the patterned WS$_2$ monolayer crystals. Moreover, the deterministic control over the polarization state of the generated nonlinear beam is demonstrated due to the crystal symmetry properties of the TMD monolayer. Our results not only provide a further understanding of light−matter interactions on the atomic scale but also pave the way toward the integration of atomically thin TMD devices into future photonic circuits for optical communication, quantum memory, and computing devices.

KEYWORDS: *nonlinear phase, second-harmonic generation, 2D material patterning, transition metal dichalcogenide monolayer*
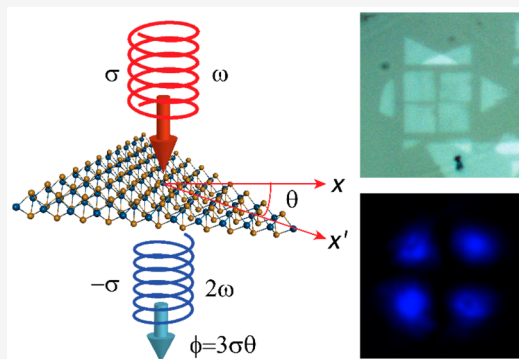
O ptical beam shaping plays an important role in tailoring how light interacts with matter, where optical frequency, polarization state, orbital angular momentum, intensity, and phase profiles of the optical beam can be precisely controlled and manipulated. Optical beam shaping in the linear optical regime has been widely used for various applications such as optical communication,[1] optical tweezers,[2−4] and microscopy.[5,6] In contrast with its linear counterpart, nonlinear beam shaping provides a compact way to perform frequency conversion and wavefront manipulation at the same time, where the converted frequency is envisioned as an extra degree of freedom for encoding information in the field of optical communication and information security.

Most nonlinear beam-shaping techniques rely on the modulation of the local phase of the nonlinear polarizability in such a way that the generated nonlinear wave interferes inside the material during its generation and propagation processes. To achieve efficient nonlinear beam conversion, it is imperative to have continuous control over the local phase of the nonlinear polarization without changing the linear optical properties of the material because induced changes in the real and imaginary parts of the refractive index of the material can affect the generation and propagation properties of the

nonlinear beam. Realizing this on the nanoscale enables on-chip photonic integration of the nonlinear devices. Nonlinear metasurfaces have been considered as the most promising platform to address the challenge of reducing the device thickness down to the subwavelength scale. Metasurfaces consist of only a single layer of plasmonic or dielectric nanostructures known as meta-atoms.[7−12] The concept of spin-rotation coupling of light is employed to engineer the local phase of the nonlinear polarizability so that spatially variant geometric phases in the generated nonlinear light across the interface of the metasurface can be obtained by selectively rotating each of the meta-atoms. Over the years, different nonlinear optical processes such as second-harmonic generation (SHG), third-harmonic generation (THG), and four-wave mixing in various types of plasmonic metasurfaces have
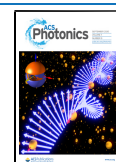
been demonstrated for flat lens imaging,[13] the generation of vortex beams and other optical beams,[14−16] optical holography,[17,18] and optical cryptography.[16] Although the thickness of plasmonic metasurfaces is as low as tens of nanometers, one major drawback is that the operating wavelength is totally dependent on the plasmonic resonance of the meta-atoms, and thus a broadband operation is not possible. Apart from this, low conversion efficiency, high absorption loss, and a small laser damage threshold are the major hindrances for their practical use. Similar approaches with dielectric metasurfaces, on the contrary, show significantly higher conversion efficiency, but the device thickness is on the order of hundreds of nanometers, which makes it hard to reach the deep subwavelength scale due to the fundamental constraints imposed by the Mie scattering.[19−22]

Recently, atomically thin nonlinear holograms using transition metal dichalcogenide (TMD) monolayers have been demonstrated, where nonlinear beam shaping at SHG wavelengths has been achieved.[23,24] High nonlinear conversion efficiency,[25] low absorption loss, and easy interfacing on the nanoscale[26] make the TMD monolayers ideal candidates for building on-chip nonlinear optical devices. The atomically thin TMD monolayers bring the device thickness down to the subnanometer scale, which is orders of magnitude lower than the thicknesses of nonlinear metasurfaces previously demonstrated. However, in these previous works,[23,24] phase and amplitude information on the desired optical beam is encoded into the binary amplitude patterns of the computer-generated hologram, without the direct modulation of the local phase profile of nonlinear material, which limits the spatial resolution of the generated beam. Motivated by that, here we show how to control the local phase of the nonlinear polarization from the TMD monolayer crystals by selective rotation of the crystals. The binary nonlinear phase modulations of 0 and π are generated from the monolayer crystals oriented along $\theta = 0$ and $60°$ to realize the nonlinear generation of Hermite−Gaussian (HG) beams at the SHG wavelength from the patterned WS$_2$ monolayer crystals. The phase information on the desired wavefront is coded on the rotated WS$_2$ monolayer crystals, which are patterned by focused ion beam milling, and the corresponding beam at the SHG wavelength is produced at the Fourier plane in the far-field. Moreover, we demonstrate the deterministic control over the polarization state of the generated nonlinear beams, which is resulted from the crystal symmetry properties of TMD monolayer. Our results not only provide a better understanding of the nonlinear light−matter interactions in TMD monolayers but also can be harnessed to realize integrated nonlinear optical devices of subnanometer scale thickness for secured information transmission, high-density optical storage, and ultrathin displays.

■ RESULTS AND DISCUSSION

We start by considering a WS$_2$ monolayer crystal where the crystal axes are rotated by an angle θ from the axes of the laboratory frame. Figure 1a shows a schematic top view of the hexagonal crystal structure of the WS$_2$ monolayer, where the yellow spheres represent the vertically separated layers of the S atoms and the blue spheres indicate the W atoms. Here the armchair direction of the WS$_2$ monolayer is oriented along the x' axis, whereas the zigzag direction comprising the broken reflection symmetry is along the y' axis. The crystals' reference axes (x', y') are rotated by an angle θ with respect to the laboratory frame axes (x, y). Now we consider an incident
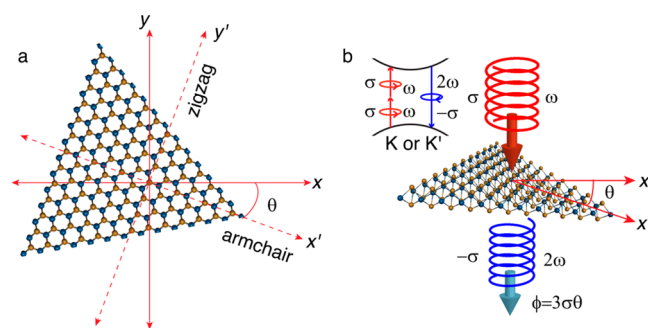

Figure 1. Illustration of the nonlinear geometric phase control for SH emission. (a) Schematic top view of the crystal structure of the WS$_2$ monolayer. The crystal's armchair and zigzag directions are indicated as x' and y' axes in the local frame. The crystal axes are rotated by an angle θ with respect to the laboratory frame (x, y). (b) Illustration of the SH emission from the rotated WS$_2$ monolayer having the acquired nonlinear geometric phase of $3\sigma\theta$ under the opposite circular polarization to that of the fundamental beam. The inset shows the schematic of the interband valley optical selection rule for SHG in the WS$_2$ monolayer.

circularly polarized fundamental beam propagating along the z direction through the WS$_2$ monolayer (Figure 1b). The continuous control of the nonlinear phases was first demonstrated by Li et al.[7] in plasmonic metasurfaces. The electric field of the fundamental beam at the angular frequency ω is expressed as $\vec{E}^{(\omega)}(\sigma) = E_0(\hat{e}_x + i\sigma\hat{e}_y)/\sqrt{2}$, where $\sigma = \pm 1$ represents left- or right-handed circular polarization (LCP or RCP) and $\hat{e}_x$ and $\hat{e}_y$ are the unit vectors along the x and y directions, respectively. Therefore, the local effective nth-order nonlinear polarization induced in the WS$_2$ monolayer can be expressed as

$$\vec{P}^{(n\omega)}(\theta, \sigma) = \epsilon_0 \cdot \overleftrightarrow{\chi}^{(n\omega)}(\theta) \cdot (\vec{E}^{(\omega)}(\sigma))^n \qquad (1)$$

where ϵ_0 is the free-space electric permittivity and $\overleftrightarrow{\chi}^{(n\omega)}(\theta)$ denotes the nth-order nonlinear susceptibility tensor of the WS$_2$ crystal at the crystal orientation angle θ. Because the WS$_2$ monolayer crystal has only subnanometer thickness, it can be assumed that the induced nonlinear polarization lies in the crystal plane and can be further decomposed into two in-plane counter-rotating components as $\vec{P}^{(n\omega)}(\theta, +\sigma)$ and $\vec{P}^{(n\omega)}(\theta, -\sigma)$, where $+\sigma$ and $-\sigma$ signify the rotation directions of nonlinear polarization components that are corotating and counter-rotating to those of the incident circular polarization, respectively. Because of the rotation of the crystal axis, the incident light acquires a spin-dependent geometric phase via spin-rotation coupling.[7] Therefore, the electric field of the fundamental beam $\vec{E}_L^{(\omega)}(\theta, \sigma)$ in the crystal's local coordinate (x', y') can be written as $\vec{E}^{(\omega)}(\sigma) \cdot e^{i\sigma\theta}$. Because the local coordinate is fixed with respect to the crystal axes at $\theta = 0°$, the nth-order nonlinear susceptibility of the WS$_2$ monolayer crystal in the local frame is simply $\overleftrightarrow{\chi}_0^{(n\omega)} = \overleftrightarrow{\chi}^{(n\omega)}(\theta = 0°)$. Thus the nth-order nonlinear polarization in the local frame (x', y') is given by

$$\vec{P}_L^{(n\omega)}(\theta, \sigma) = \epsilon_0 \cdot \overleftrightarrow{\chi}_0^{(n\omega)} \cdot (\vec{E}^{(\omega)}(\sigma))^n \cdot e^{in\sigma\theta} \qquad (2)$$

Again, the induced nonlinear polarization can be written as a superposition of two in-plane counter-rotating components in the local frame as $\vec{P}_L^{(n\omega)}(\theta, +\sigma) \propto e^{in\sigma\theta}$ and $\vec{P}_L^{(n\omega)}(\theta, -\sigma) \propto e^{in\sigma\theta}$. Finally, by transforming from the local frame (x', y') back to
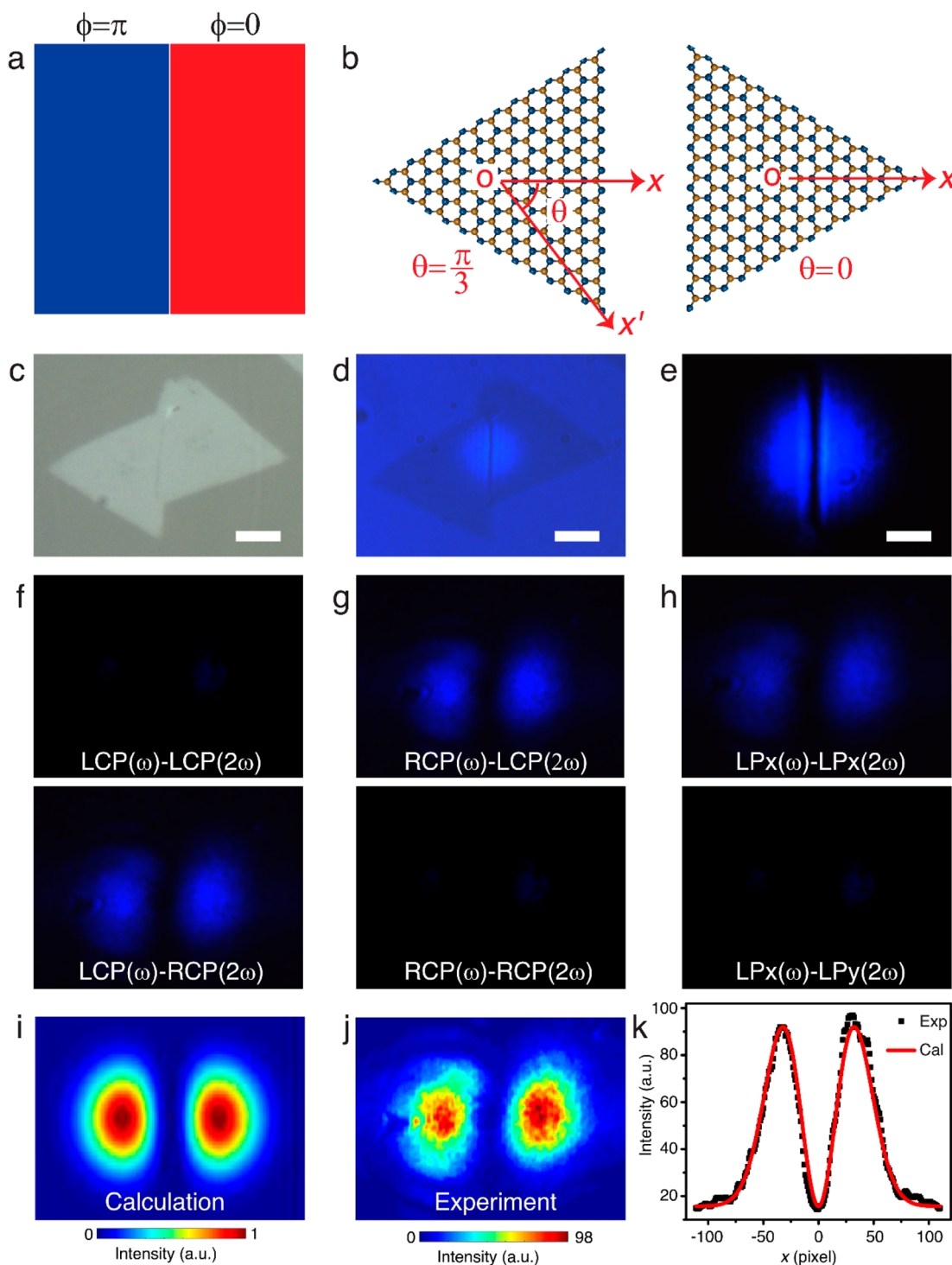
Figure 2. Nonlinear generation of the second-harmonic HG_{10} beam. (a) Effective phase profile of SH emission required for the generation of the HG_{10} beam. (b) Schematic view of two WS_2 monolayer crystals oriented along $\theta = 0°$ and $\theta = 60°$, which induce the nonlinear geometric phase shifts of 0 and π in the SHG response, respectively. (c) Reflection microscope image of the WS_2 monolayer structure, where two single crystals with opposite armchair orientations are formed naturally right next to each other during the CVD growth. (d) Bright-field transmission microscope image showing the SH emission from the illuminated area of the WS_2 monolayer structure excited by the fundamental beam at $\lambda = 900$ nm. Scale bar is 20 μm. The fundamental beam has a symmetric Gaussian profile. (e) Zoomed-in dark field image of SH emission at the sample plane from the illuminated area of the WS_2 monolayer structure when the background white light is turned off. Scale bar is 10 μm. (f) Polarization-resolved far-field images of the generated HG_{10} beam at the SH wavelength of 450 nm excited by the LCP fundamental beam. (g) Polarization-resolved far-field SH images in the case of the RCP fundamental excitation. (h) Far-field SH images of the generated HG_{10} beam in the case of the LP excitation along the x direction. LPx and LPy represent the linear polarization along the x and y directions, respectively. (i) Theoretically calculated beam profile of an ideal HG_{10} beam. (j) Colormap reproduction of the generated HG_{10} beam. (k) Measured intensity line profile of the generated HG_{10} beam (black data points) and calculated intensity line profile of the ideal HG_{10} beam (red solid curve).

the laboratory frame (x, y), the nonlinear polarization components take the form of[7]

$$\vec{P}^{(n\omega)}(\theta, +\sigma) = \vec{P}_L^{(n\omega)}(\theta, +\sigma)\cdot e^{-i\sigma\theta} \propto e^{i(n-1)\sigma\theta}$$

$$\vec{P}^{(n\omega)}(\theta, -\sigma) = \vec{P}_L^{(n\omega)}(\theta, -\sigma)\cdot e^{i\sigma\theta} \propto e^{i(n+1)\sigma\theta} \quad (3)$$

Now, the electric field of the nth-order harmonic generation can be expressed as $\vec{E}^{(n\omega)} \propto \vec{P}^{(n\omega)}$. Hence the nth-order harmonic emission contains two circularly polarized components with different nonlinear geometric phases depending on the rotation angle of the crystal, where $\vec{E}^{(n\omega)}(\theta, +\sigma)$ with the same circular polarization as the fundamental beam has the phase of $(n-1)\sigma\theta$, whereas $\vec{E}^{(n\omega)}(\theta, -\sigma)$ with the opposite circular polarization exhibits the phase of $(n+1)\sigma\theta$. However, on the basis of the rotational symmetry of the crystal and the order of the harmonic generation, either one or both of the circular polarization components can be present.

The WS$_2$ monolayer belongs to the D_{3h} crystal group with three-fold rotational symmetry. Under the excitation from a circularly polarized fundamental beam, a spin-flipped SHG is observed in any conventional nonlinear crystals with three-fold rotational symmetry. Such circular polarization SHG selection rule arises from the rotational symmetry requirement of the crystal for the conservation of total angular momentum during the photon–lattice interaction, where the lattice supplies the extra angular momentum to the second-harmonic (SH) photons. However, in the WS$_2$ monolayer, like any other TMD monolayers under two-photon fundamental excitation above the band gap, the SHG selection rule is valley-dependent. The presence of strong spin–orbit coupling in the WS$_2$ monolayer results in the formation of energy-degenerate valleys in momentum space at the corners of the first Brillouin zone (and points). The fact that these inequivalent valleys (K and K') are composed of opposite spin states leads to the selective absorption or emission of the LCP or RCP photons.[27,28] Thereby, the SHG selection rule is modified by introducing the valley angular momentum (VAM) and can be written as[29,30]

$$\Delta\sigma = \Delta\tau + 3N \quad (N = \pm 1) \quad (4)$$

where $\Delta\sigma$ signifies the change in the circular polarization state of photons, $\Delta\tau$ is the change in the valley quantum number, and the term $3N$ represents the change in the lattice angular momentum due to the three-fold rotational symmetry of the crystal. The electronic transition from the valence band to the conduction band in the K or K' valley requires a $-1\hbar$ or $+1\hbar$ change in the angular momentum. If we consider a SHG process under LCP excitation ($\sigma = +1$), then the absorption of two fundamental photons in the K valley causes a $+2\hbar$ change in spin angular momentum and an excess angular momentum of $+3\hbar$ in the crystal lattice. Thus the resulting SH photon is emitted with the opposite circular polarization state ($\sigma = -1$). A schematic of the underlying mechanism is shown in the inset of Figure 1b. Similarly, under time reversal, the absorption of two RCP fundamental photons at K' valley results in the emission of one LCP SH photon. Therefore, the emitted SH photons from the WS$_2$ monolayer with the crystal rotation angle θ will only acquire the nonlinear geometric phase of $3\sigma\theta$ with the opposite circular polarization of $-\sigma$, as illustrated in Figure 1b. By gradually varying the crystal rotation angle θ, the continuous-phase manipulation of the SH emission covering the whole range from 0 to 2π will be achieved for nonlinear

beam-shaping applications. In the case of the linearly polarized (LP) excitation, the incident electric field of the fundamental beam can be represented in the circular polarization basis as $\vec{E}^{(\omega)} = |\tilde{E}^{(\omega)}(\sigma = +1)|\hat{e}_{+1} + |\tilde{E}^{(\omega)}(\sigma = -1)|\hat{e}_{-1}$, where $\hat{e}_{\pm 1} = \frac{1}{\sqrt{2}}(\hat{e}_x \pm i\hat{e}_y)$ are the unit vectors and $\tilde{E}^{(\omega)}(\sigma = +1)$ and $\tilde{E}^{(\omega)}(\sigma = -1)$ are the corresponding light fields of the LCP and RCP components, respectively. Because the SH emission from the WS$_2$ monolayer is spin-flipped, it is clear that the acquired nonlinear geometric phase of the SH electric field under linearly polarized fundamental excitation will again be 3θ for the crystal orientation angle θ.

To verify the theoretical predictions, at first, a simple example of nonlinear beam shaping with binary phase manipulation rather than continuous-phase manipulation is demonstrated through the generation of the first-order Hermite–Gaussian (HG$_{10}$) beam. To produce the SH beam at the far-field, the required phase information needs to be encoded into the converted SH photons from the nonlinear structure. By exciting the nonlinear structure with a fundamental Gaussian beam, the SH HG$_{10}$ beam can be generated from the following phase profile in the SH response[31]

$$\phi(x, y) = \begin{cases} 0 & x \in \left[0, \dfrac{a}{2}\right] \\[2mm] \pi & x \in \left[0, -\dfrac{a}{2}\right] \end{cases} \quad (5)$$

where a is the diameter of the illuminating Gaussian pump beam. Figure 2a shows the required binary phase profile for the generation of the SH HG$_{10}$ beam. The zero geometric phase shift in the SH emission is induced when the armchair axis of the WS$_2$ monolayer crystal is oriented along the x direction. (See Figure 2b.) As the armchair axis of the crystal is rotated by an angle $\theta = \frac{\pi}{3}$, the geometric phase acquired by the SH photons is $\phi = \pi$ (Figure 2b). Hence, the required phase profile shown in Figure 2a can be obtained by arranging two identical monolayer crystals with the orientation angles 0° and 60° right next to each other. In the experiment, the WS$_2$ monolayer triangles grown on c-cut (001) sapphire substrate by the low-pressure chemical vapor deposition (CVD) (2D semiconductors) are used. Figure 2c shows the reflection optical microscope image of the WS$_2$ monolayer structure consisting of two oppositely oriented crystals, which are arranged side by side during the CVD growth. Figure 2d is a bright-field transmission microscope image showing the SH emission from the illuminated area of the WS$_2$ monolayer structure when it is excited with a fundamental Gaussian beam of wavelength $\lambda = 900$ nm. An appropriate optical bandpass filter allowing the SH wavelength of 450 nm and blocking the fundamental wavelength is inserted in front of the imaging charge-coupled device (CCD) camera while capturing the image. A zoomed-in dark-field image of the SH emission is presented in Figure 2e. The absence of an SHG signal at the grain boundary of two crystals is due to the destructive interference of the SHG fields generated from the neighboring single crystals with the 0 and π phases.[32] To acquire the SH images, the pump power is set at 5 mW, and the beam spot size is 20 μm. The generated SH beam profile in the far field is characterized using a Fourier microscopy system (see the Methods for the details of the system) for different
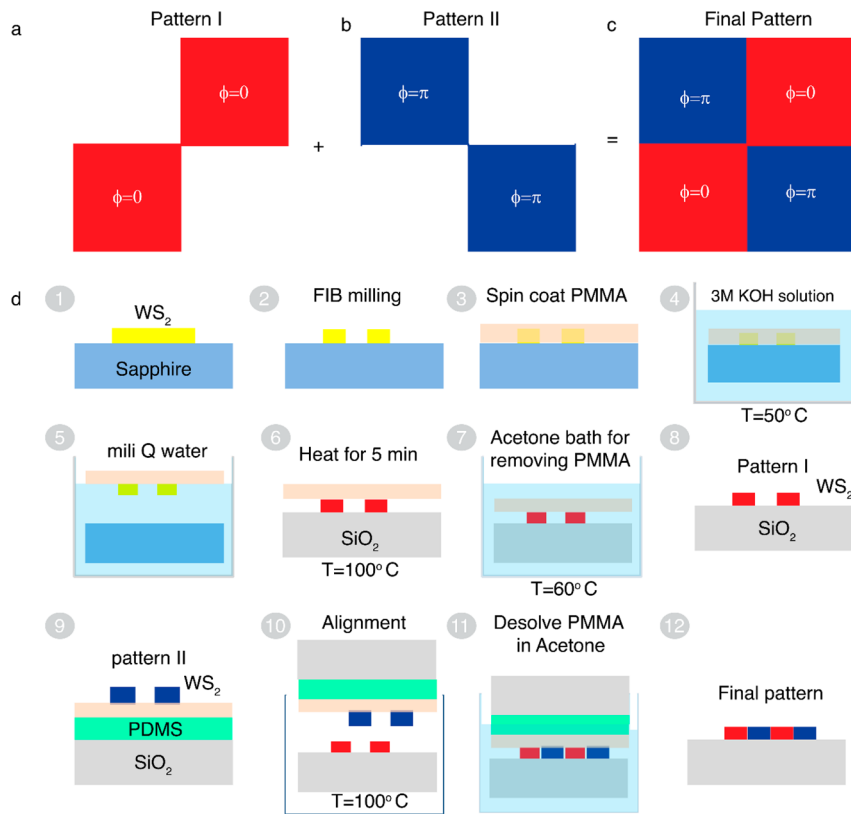
Figure 3. Preparation of the patterned WS_2 monolayer crystals with binary phase modulation for the generation of the HG_{11} beam. Two individual binary patterns representing the phase modulations of (a) $\phi = 0$ and (b) $\phi = \pi$ are combined to form the final pattern (c) with the required phase profile to generate the HG_{11} beam. (d) Schematic illustration of the step-by-step nanofabrication process to make the final combined WS_2 monolayer patterns.

combinations of input and output polarizations. Figure 2f shows that the generated SH HG_{10} beam is RCP polarized when the WS_2 monolayer structure is excited with the LCP fundamental Gaussian beam, whereas Figure 2g shows that the opposite scenario is observed in the case of the RCP fundamental beam excitation. Figure 2h shows that the generated SH HG_{10} beam has the same linear polarization as the fundamental beam polarized along the x direction. All of these results are in agreement with the theoretical predictions. To further characterize the generated HG_{10} beam, we compare the measured beam profile with the theoretical calculation. The intensity profile of an ideal HG_{10} beam can be expressed as

$$I_{10}(x,y) \propto \left[E_0 \cdot \frac{w_0}{w(z)} \cdot H_1\left(\frac{\sqrt{2}x}{w(z)}\right) \cdot H_0\left(\frac{\sqrt{2}y}{w(z)}\right) \cdot \exp\left(-\frac{x^2+y^2}{w(z)^2}\right) \right]^2, \text{ where}$$

E_0 is the field amplitude, w_0 is the waist radius, $w(z)$ is the waist radius at which the field amplitudes fall to $1/e$ of their axial values, and $H_m(u)$ is the mth-order Hermite polynomial. Figure 2i shows the theoretically calculated 2D intensity profile of an ideal HG_{10} beam. In Figure 2j, the measured HG_{10} beam shown in Figure 2f is reproduced with the same colormap as Figure 2i, where it can be seen that the experimental beam profile is close to the calculated one. Figure 2k further plots the measured line profile of the generated HG_{10} beam, which agrees well with the calculated line profile of ideal HG_{10} beam.

Next, the idea of the binary phase manipulation is further extended to design a phase-modulation-based nonlinear beam-shaping device using the patterned WS_2 monolayer crystals by demonstrating the generation of the SH HG_{11} beam. A nonlinear medium illuminated with a Gaussian fundamental

beam can generate an SH HG_{11} beam if the SH emission can acquire the phase profile given by[31]

$$\phi(x, y)$$
$$= \begin{cases} 0 & (x, y) \in \left(\left[0, \frac{a}{2}\right], \left[0, \frac{a}{2}\right]\right); \ (x, y) \in \left(\left[0, -\frac{a}{2}\right], \left[0, -\frac{a}{2}\right]\right) \\ \pi & (x, y) \in \left(\left[0, -\frac{a}{2}\right], \left[0, \frac{a}{2}\right]\right); \ (x, y) \in \left(\left[0, \frac{a}{2}\right], \left[0, -\frac{a}{2}\right]\right) \end{cases}$$

$$(6)$$

As shown in Figure 3, the required phase profile (Figure 3c) can be designed by combining two separate binary patterns containing the phase modulations of $\phi(x, y) = 0$ (Figure 3a) and $\phi(x, y) = \pi$ (Figure 3b). Thereby, the nonlinear structure can be formed by patterning two individual WS_2 triangles with appropriate orientation angles and transferring the patterns all together. The step-by-step nanofabrication process to make the final combined WS_2 monolayer patterns is illustrated in Figure 3d. First, the sapphire substrate with the CVD-grown WS_2 monolayer crystals is cut into two pieces. Then, the binary pattern representing the phase modulation of $\phi(x, y) = 0$ (Figure 3a) is patterned on a monolayer crystal oriented along $\theta = 0°$ on one piece of sapphire substrate using focused ion beam (FIB) milling, while the complementary binary pattern with $\phi(x, y) = \pi$ (Figure 3b) is written on a monolayer crystal oriented along $\theta = 60°$ on the other piece of sapphire substrate. More details of the FIB milling are included in the Methods section. The binary pattern with the phase modulation of $\phi(x, y) = 0$ is first transferred onto a glass substrate following a polymethyl methacrylate (PMMA)-assisted transfer meth-
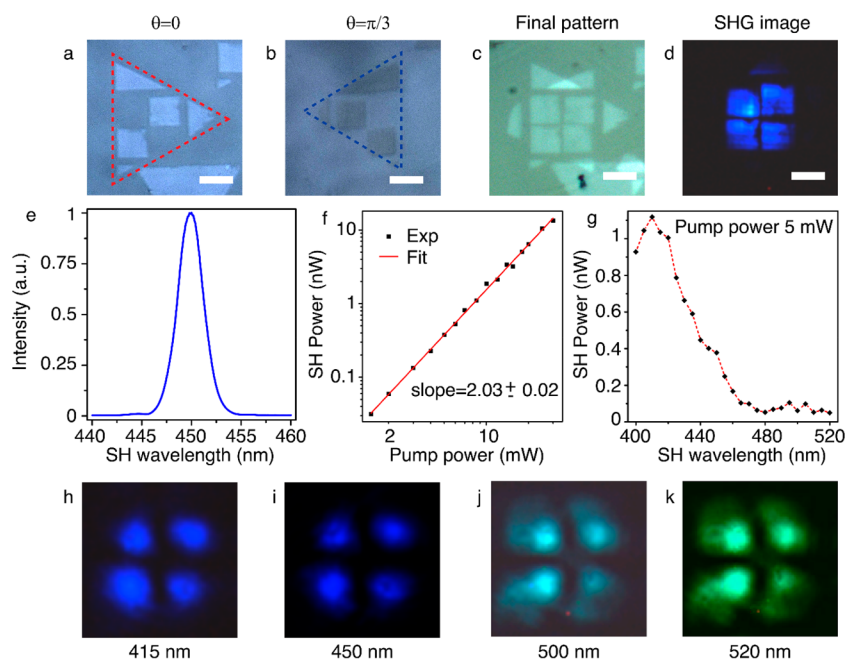
Figure 4. Second-harmonic generation of the HG_{11} beam. (a) Reflection microscope image of the patterned WS_2 monolayer triangle oriented along $\theta = 0°$ on a glass substrate, representing the $\phi = 0$ phase modulation. (b) Reflection image of the patterned WS_2 monolayer triangle oriented along $\theta = 60°$ on the PDMS−PMMA film, representing the $\phi = \pi$ phase modulation. (c) Reflection image of the final combined WS_2 monolayer pattern on a glass substrate to generate the HG_{11} beam after completion of the transfer process. (d) Transmission microscope image of the SH emission from the final combined pattern at the fundamental wavelength of 900 nm. Scale bars are 10 μm. (e) SHG spectrum from the final combined pattern at the fundamental wavelength of 900 nm. (f) Double log-scale plot of the measured average SH power from the final combined pattern as a function of the average incident pump power at 900 nm excitation. (g) Evolution of the average SH power as a function of the SH wavelength with the incident pump power of 5 mW. (h−k) Far-field SH images of the generated HG_{11} beam at the SH wavelengths of 415, 450, 500, and 520 nm, respectively.

od.[33,34] After spin coating PMMA (950 kDa) on the WS_2 monolayer sample, it is heated to 130° for 2 min. Polymer strips at the edge of the sample are then scratched out using a blade to facilitate smooth lift-off. Next, the sample is immersed in 3 M potassium chloride (KOH) solution and kept at 50 °C for 1.5 to 2 h. After sapphire etching by KOH, the PMMA film containing the patterned WS_2 crystal is washed with deionized (DI) water two times for 10 min at each step to remove the residual KOH. Then, the PMMA film is fished out of the DI water with a glass slide and placed on a hot plate at 100 °C for 10 min. Once the film dries up and the crystals have strong adhesion to the glass substrate, the PMMA is removed by immersing the sample in acetone at 50 °C temperature for 30 min. Finally the sample is rinsed with DI water and isopropyl alcohol (IPA) to remove residual acetone and dried up by flowing N_2 gas on it. Figure 4a displays a reflection microscope image of a patterned WS_2 monolayer crystal with the orientation angle $\theta = 0°$ after transferring it on the glass substrate, representing the phase modulation of $\phi(x, y) = 0$.

Next, the complementary binary pattern with the phase modulation of $\phi(x, y) = \pi$ is transferred onto a PMMA film from the other piece of sapphire substrate following the same KOH etching steps. The PMMA-WS_2 film is flipped upside down and transferred onto a piece of a polydimethylsiloxane (PDMS) film that is placed on a glass slide. After drying up the sample by blowing N_2 gas on it, the final transfer step is performed. Figure 4b gives a reflection microscope image of the patterned WS_2 monolayer crystal with the rotation angle $\theta = 60°$ transferred on the PMMA film, giving $\phi(x, y) = \pi$ phase modulation. Now, the receiving WS_2 crystal on the glass substrate shown in Figure 4a is placed in a Petri dish that is

attached to an *xyz*-translation stage. A second *xyz* stage is used to hold the other glass slide containing the PMMA-WS_2 film on PDMS. Once these two patterned WS_2 crystals are properly aligned with the help of an optical microscope, two glass substrates approach each other until they touch. To ensure proper adhesion, the lower glass substrate is heated to 80−100 °C using a Peltier heating module. Acetone is then slowly poured into the Petri dish while keeping the pressure from the top glass substrate intact. When the acetone slowly penetrates through the PDMS and starts dissolving PMMA, a successful transfer is confirmed immediately after the two translation stages are slowly detached. The sample is kept in acetone for another 20 min to ensure the complete removal of PMMA. Finally, the sample is again rinsed with DI water and IPA, and dried with N_2 gas. Figure 4c shows the reflection microscope image of the final combined WS_2 monolayer pattern on the glass substrate after the completion of the entire fabrication process. To efficiently fabricate the patterned structures with continuous phase control, precision nanopositioning systems can be further utilized to achieve the precise alignment control of multiple patterned monolayers with different crystal rotation angles. Another potential approach could be the direct growth of monolayer crystals with spatially controlled crystal axis orientations.

Figure 4d displays the captured transmission microscope image of the SH emission from the final combined WS_2 monolayer pattern excited by the fundamental beam at the wavelength of $\lambda = 900$ nm, with the beam spot size of 20 μm and the incident pump power of 5 mW. Figure 4e plots the SHG spectrum from the final combined pattern showing an intensity peak at 450 nm that is exactly half of the fundamental
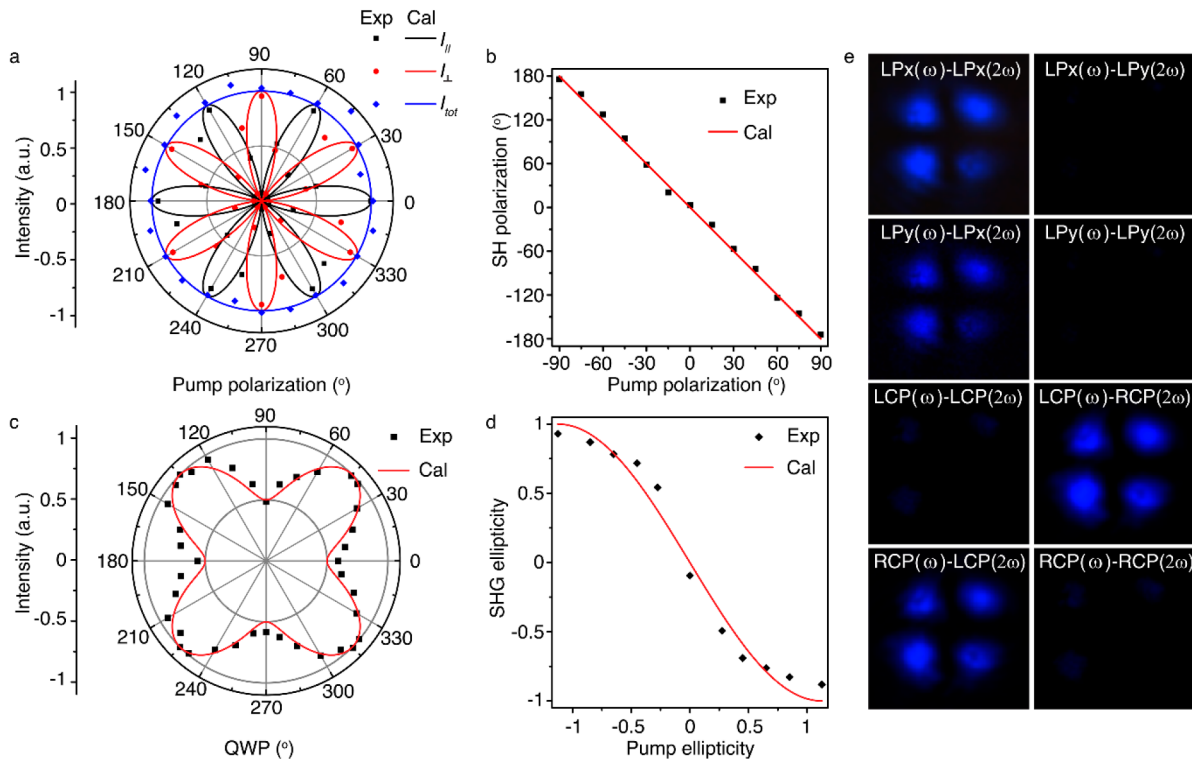
Figure 5. Dependence the intensity and polarization state of the generated SH HG_{11} beam on the polarization state of the fundamental beam. (a) Polar plot of the parallel (black) and perpendicular (red) components along with the total (blue) intensity of the generated SH HG_{11} beam as a function of the linear polarization angle of the fundamental beam. (b) Evolution of the linear polarization angle of the SH HG_{11} beam as a function of that of the fundamental beam. (c) Plot of the intensity of the SH HG_{11} beam as a function of the QWP angle. (d) Evolution of the ellipticity of the SH HG_{11} beam as a function of the ellipticity of the fundamental beam. (e) Far-field SH images of the generated HG_{11} beam for different combinations of the incident pump polarization and the output SH polarization, manifesting the nonlinear polarization selection rule. LPx and LPy represent the linear polarization along the x and y directions, respectively.

wavelength. The SH emission is characterized in Figure 4f by plotting the log−log variation of the collected SHG signal as a function of the incident pump power at 900 nm excitation. The power scaling of the SHG follows the expected quadratic dependence very well. The broadband operation is further demonstrated for the SH wavelength range between 400 and 520 nm. The evolution of SH power as a function of SH wavelength is plotted in Figure 4g, with the beam spot size of 20 μm and the pump power of 5 mW. The conversion efficiency (CE) of nonlinear beam generation can be assessed by the ratio of the average SH power and the average pump power. The maximum CE of 2.6×10^{-7} is obtained at the SH wavelength of 415 nm. Figure 4h−k shows the far-field SH images of the generated HG_{11} beam at SH wavelengths of 415, 450, 500, and 520 nm, respectively.

Furthermore, the dependence of the polarization properties of the generated SH HG_{11} beam on the various polarization states of the fundamental beam is investigated. An arbitrarily polarized fundamental beam can be represented as a linear superposition of the LCP and RCP components as

$$\vec{E}^{(\omega)} = |\tilde{E}^{(\omega)}(\sigma = +1)|e^{+i\theta_P}\hat{e}_{+1} + |\tilde{E}^{(\omega)}(\sigma = -1)|e^{-i\theta_P}\hat{e}_{-1} \tag{7}$$

where θ_p is the azimuthal angle of the polarization plane with respect to the armchair axis of the WS_2 monolayer crystal. The armchair axis corresponds to the mirror symmetry of the crystal that has three-fold rotational symmetry, so that a 60° rotation in the crystal will give the opposite armchair direction. Hence, θ_p is the same for both of the patterned WS_2 monolayer

crystals with rotation angles of $\theta = 0°$ and $\theta = 60°$. The ellipticity of the fundamental beam polarization can be given as $\epsilon = \frac{(|\tilde{E}^{(\omega)}(\sigma = -1)| - |\tilde{E}^{(\omega)}(\sigma = +1)|)}{(|\tilde{E}^{(\omega)}(\sigma = -1)| + |\tilde{E}^{(\omega)}(\sigma = +1)|)}$. The SH electric field is then written as

$$\vec{E}^{(2\omega)} \propto \varepsilon_0 \chi^{(2\omega)}[|\tilde{E}^{(\omega)}(\sigma = -1)|^2 e^{-2i\theta_P}\hat{e}_{+1} + |\tilde{E}^{(\omega)}(\sigma = +1)|^2 e^{+2i\theta_P}\hat{e}_{-1}] \tag{8}$$

Therefore, the polarization orientation $\theta_{2\omega}$ of the SH beam becomes

$$\theta_{2\omega} = -2\theta_p \tag{9}$$

whereas the ellipticity of the SH beam is

$$\epsilon_{2\omega} = \frac{|\tilde{E}^{(\omega)}(\sigma = +1)|^2 - |\tilde{E}^{(\omega)}(\sigma = -1)|^2}{|\tilde{E}^{(\omega)}(\sigma = +1)|^2 + |\tilde{E}^{(\omega)}(\sigma = -1)|^2} = -\frac{2\epsilon}{1 + \epsilon^2} \tag{10}$$

It is clear that in the case of the linearly polarized fundamental excitation ($\epsilon = 0$), the generated SH beam is also linearly polarized, and the polarization orientation $\theta_{2\omega}$ of the SH beam can be controlled by the linear polarization angle θ_p of the fundamental beam while keeping the amplitude of the SHG signal constant. However, in the case of the elliptically polarized fundamental excitation ($\epsilon \neq 0$), apart from controlling the polarization parameters, the intensity of the SH beam can also be modulated. The relation between the intensity of the SH beam and the ellipticity of the fundamental beam can be given as

$$I^{(2\omega)} \propto \left(1 + \sin^2(2\tan^{-1}\epsilon)\right) \tag{11}$$

The evolution of the intensity of the SH HG_{11} beam as a function of the linear polarization angle θ_p of the fundamental beam is plotted in the blue curve in Figure 5a, where the polarization of the incident beam is changed using a rotating half-wave plate. It is evident that the intensity of the SH beam remains almost the same for any incident linear polarization angle. The black and red curves in Figure 5a show the dependence of the parallel and perpendicular components of the SH HG_{11} beam as a function of the incident linear polarization angle θ_p, respectively. These results indicate that the generated SH HG_{11} beam is linearly polarized. To confirm the prediction of eq 9, the ellipticity $\epsilon_{2\omega}$ and polarization orientation $\theta_{2\omega}$ of the SH HG_{11} beam are also determined for different linear polarization angles θ_p of the fundament excitation by measuring the Stokes parameters of the SH signal as $S_0 = |E_x^{(2\omega)}|^2 + |E_y^{(2\omega)}|^2$, $S_1 = |E_x^{(2\omega)}|^2 - |E_y^{(2\omega)}|^2$, $S_2 = 2Re[E_x^{(2\omega)}E_y^{(2\omega)}]$, and $S_3 = -2Im[E_x^{(2\omega)}E_y^{(2\omega)}]$. The ellipticity and polarization orientation of the SH beam are then obtained as $\epsilon_{2\omega} = \tan\left(\frac{1}{2}\sin^{-1}\frac{S_3}{S_0}\right)$ and $\theta_{2\omega} = \frac{1}{2}\tan^{-1}\frac{S_2}{S_1}$, respectively.

Figure 5b plots the variation of the measured polarization angle of the generated SH HG_{11} beam as a function of the linear polarization angle of the pump beam, where the relation of $\theta_{2\omega} = -2\theta_p$ is clearly observed. Moreover, the influence of the elliptical polarization of the fundamental beam on the polarization state of the SH HG_{11} beam is verified. Figure 5c characterizes the dependence of the SH intensity on the ellipticity of the fundamental beam. The desired incident elliptical polarization is obtained by placing a linear polarizer along the x axis ($\theta_p = 0°$) and a rotating quarter-wave plate (QWP). Depending on the rotation angle β of the fast axis of the QWP with respect to the linear polarizer, the ellipticity of the fundamental beam is determined by $\epsilon = \tan \beta$, where the fundamental beam varies from being linearly polarized for $\beta = 0° + m\cdot90°$ to circularly polarized for $\beta = 45° + m\cdot90°$. The observed nearly doubled intensity of the generated SH HG_{11} beam under circularly polarized excitation compared with that of the linearly polarized excitation is in good agreement with the theoretical prediction of eq 11. The ellipticity $\epsilon_{2\omega}$ of the SH HG_{11} beam is then measured as a function of the ellipticity ϵ of the fundamental beam. Note that ϵ is gradually varied from -1 to $+1$ by changing β from -45 to $+45°$, which signify the RCP and LCP, respectively. As shown in Figure 5d, the measured $\epsilon_{2\omega}$ always has the opposite sign to that of ϵ, which is consistent with the theoretical prediction from eq 10. The slight deviation of the experimental data from the theoretical calculation may be attributed to the slight misalignments of the monolayer patterns during the nanofabrication process. In Figure 5e, the far-field SH images of the generated HG_{11} beam for different combinations of the incident pump polarization and the output SH polarization further demonstrate the deterministic control over the polarization states of the SH beam and manifest the nonlinear polarization selection rule in the patterned WS_2 monolayer crystals.

CONCLUSIONS

In summary, we have introduced nonlinear phase manipulation for the SH emission from the WS_2 monolayer crystals through spin-rotation coupling, where the continuous nonlinear geometric phase of the SH response can be precisely controlled by rotating the crystal axis with the specified angle. We validate

the concept by demonstrating the binary phase modulation consisting of the nonlinear phases 0 and π on the patterned WS_2 monolayer crystals for the nonlinear generation of the HG_{10} and HG_{11} beams at the SH frequency. The conversion efficiency of nonlinear beam generation is notably higher than that of the previously reported nonlinear plasmonic metasurfaces. Furthermore, we show that the rotational symmetry associated with the TMD monolayer provides deterministic control over the output polarization state of the generated SH beam. Unlike the conventional nonlinear crystals and metasurfaces, the valley dependence of the circular polarization SHG selection rule on the TMD monolayers makes the SHG signal immune to the presence of the impurity, defects, and phonon scattering. Moreover, the gradual rotation of the TMD monolayer crystal over an interface will provide continuous control over the nonlinear geometric phase covering the entire range from 0 to 2π for other complex nonlinear beam-shaping and holographic imaging applications. In general, our concept of the nonlinear phase manipulation from the WS_2 monolayer can be further extended to other TMDs and other types of 2D materials for not only the SHG process but also the third-harmonic and high-harmonic generations. The TMD monolayers enable the thickness of nonlinear optical devices down to the subnanometer scale, which is orders of magnitude lower than the thicknesses of the previously reported nonlinear metasurfaces. Our work can be harnessed to build atomically thin integrated on-chip photonic and quantum devices used for optical communications, quantum information processing, optical data security and storage, and ultrathin displays.

METHODS

Sample Preparation. The single-crystal WS_2 monolayer triangles are grown on c-cut (0001) sapphire substrate by low-pressure CVD (2D Semiconductors). The binary patterns on the WS_2 monolayer are etched by focused ion beam milling (FEI Helios Nanolab 600, Ga^+ source, 30 kV, 1.5 pA). The dose, dwell time, and astigmatism of the Ga^+ ion beam are optimized to maximize the ion milling accuracy and minimize the Ga^+ ion contamination to the WS_2 monolayer. The detailed step-by-step nanofabrication process to make the final combined WS_2 monolayer patterns is illustrated in Figure 3.

Optical Setup. A femtosecond laser pulse at the fundamental wavelength from a tunable Ti:Sapphire oscillator (Coherent Chameleon, wavelength range 690−1040 nm, repetition rate 80 MHz, pulse width <100 fs) goes through a linear polarizer and a half-wave plate or a quarter-wave plate and then focuses on the WS_2 monolayer pattern with a 4× objective lens (NA = 0.12). The SH emission from the WS_2 monolayer pattern is collected by a 20× objective (NA = 0.42). After transmitting through a short-pass filter to block the transmitted fundamental laser beam, the SH images are recorded in either k-space or real space with a color CCD camera. For the spectral characterization, the transmitted SH emission is routed toward a spectrometer (iHR520, Jobin Yvon). To characterize the polarization state of the SH emission, another quarter-wave plate and linear polarizer set is inserted in front of the CCD camera to measure the Stokes parameters.

AUTHOR INFORMATION

Corresponding Authors

Jie Gao − *Department of Mechanical and Aerospace Engineering, Missouri University of Science and Technology, Rolla, Missouri*

65409, United States; ● orcid.org/0000-0003-0772-4530;
Email: gaojie@mst.edu

Xiaodong Yang − *Department of Mechanical and Aerospace Engineering, Missouri University of Science and Technology, Rolla, Missouri 65409, United States;* ● orcid.org/0000-0001-9031-3155; Email: yangxia@mst.edu

Author

Arindam Dasgupta − *Department of Mechanical and Aerospace Engineering, Missouri University of Science and Technology, Rolla, Missouri 65409, United States*

Complete contact information is available at:
https://pubs.acs.org/10.1021/acsphotonics.0c00819

Notes

The authors declare no competing financial interest.

■ REFERENCES

(1) Wang, J.; Yang, J.-Y.; Fazal, I. M.; Ahmed, N.; Yan, Y.; Huang, H.; Ren, Y.; Yue, Y.; Dolinar, S.; Tur, M.; Willner, A. E. Terabit free-space data transmission employing orbital angular momentum multiplexing. *Nat. Photonics* **2012**, *6*, 488−496.

(2) Dholakia, K.; Čižmár, T. Shaping the future of manipulation. *Nat. Photonics* **2011**, *5*, 335−342.

(3) Padgett, M.; Bowman, R. Tweezers with a twist. *Nat. Photonics* **2011**, *5*, 343−348.

(4) Curtis, J. E.; Koss, B. A.; Grier, D. G. Dynamic holographic optical tweezers. *Opt. Commun.* **2002**, *207*, 169−175.

(5) Klar, T. A.; Engel, E.; Hell, S. W. Breaking Abbe's diffraction resolution limit in fluorescence microscopy with stimulated emission depletion beams of various shapes. *Phys. Rev. E: Stat. Phys., Plasmas, Fluids, Relat. Interdiscip. Top.* **2001**, *64*, No. 066613.

(6) Vettenburg, T.; Dalgarno, H. I. C.; Nylk, J.; Coll-Lladó, C.; Ferrier, D. E. K.; Čižmár, T.; Gunn-Moore, F. J.; Dholakia, K. Light-sheet microscopy using an Airy beam. *Nat. Methods* **2014**, *11*, 541−544.

(7) Li, G.; Chen, S.; Pholchai, N.; Reineke, B.; Wong, P. W. H.; Pun, E. Y. B.; Cheah, K. W.; Zentgraf, T.; Zhang, S. Continuous control of the nonlinearity phase for harmonic generations. *Nat. Mater.* **2015**, *14*, 607−612.

(8) Segal, N.; Keren-Zur, S.; Hendler, N.; Ellenbogen, T. Controlling light with metamaterial-based nonlinear photonic crystals. *Nat. Photonics* **2015**, *9*, 180−184.

(9) Chen, S.; Li, G.; Cheah, K. W.; Zentgraf, T.; Zhang, S. Controlling the phase of optical nonlinearity with plasmonic metasurfaces. *Nanophotonics* **2018**, *7*, 1013−1024.

(10) Tymchenko, M.; Gomez-Diaz, J. S.; Lee, J.; Nookala, N.; Belkin, M. A.; Alù, A. Gradient Nonlinear Pancharatnam-Berry Metasurfaces. *Phys. Rev. Lett.* **2015**, *115*, 207403.

(11) Li, G.; Zhang, S.; Zentgraf, T. Nonlinear photonic metasurfaces. *Nat. Rev. Mater.* **2017**, *2*, 17010.

(12) Konishi, K.; Higuchi, T.; Li, J.; Larsson, J.; Ishii, S.; Kuwata-Gonokami, M. Polarization-Controlled Circular Second-Harmonic Generation from Metal Hole Arrays with Threefold Rotational Symmetry. *Phys. Rev. Lett.* **2014**, *112*, 135502.

(13) Schlickriede, C.; Waterman, N.; Reineke, B.; Georgi, P.; Li, G.; Zhang, S.; Zentgraf, T. Imaging through Nonlinear Metalens Using Second Harmonic Generation. *Adv. Mater.* **2018**, *30*, 1703843.

(14) Chen, Y.; Yang, X.; Gao, J. Spin-Selective Second-Harmonic Vortex Beam Generation with Babinet-Inverted Plasmonic Meta-surfaces. *Adv. Opt. Mater.* **2018**, *6*, 1800646.

(15) Keren-Zur, S.; Avayu, O.; Michaeli, L.; Ellenbogen, T. Nonlinear Beam Shaping with Plasmonic Metasurfaces. *ACS Photonics* **2016**, *3*, 117−123.

(16) Walter, F.; Li, G.; Meier, C.; Zhang, S.; Zentgraf, T. Ultrathin Nonlinear Metasurface for Optical Image Encoding. *Nano Lett.* **2017**, *17*, 3171−3175.

(17) Ye, W.; Zeuner, F.; Li, X.; Reineke, B.; He, S.; Qiu, C.-W.; Liu, J.; Wang, Y.; Zhang, S.; Zentgraf, T. Spin and wavelength multiplexed nonlinear metasurface holography. *Nat. Commun.* **2016**, *7*, 11930.

(18) Almeida, E.; Bitton, O.; Prior, Y. Nonlinear metamaterials for holography. *Nat. Commun.* **2016**, *7*, 12533.

(19) Wang, L.; Kruk, S.; Koshelev, K.; Kravchenko, I.; Luther-Davies, B.; Kivshar, Y. Nonlinear Wavefront Control with All-Dielectric Metasurfaces. *Nano Lett.* **2018**, *18*, 3978−3984.

(20) Gao, Y.; Fan, Y.; Wang, Y.; Yang, W.; Song, Q.; Xiao, S. Nonlinear Holographic All-Dielectric Metasurfaces. *Nano Lett.* **2018**, *18*, 8054−8061.

(21) Sain, B.; Meier, C.; Zentgraf, T. Nonlinear optics in all-dielectric nanoantennas and metasurfaces: a review. *Adv. Photonics* **2019**, *1*, No. 024002.

(22) Liu, B.; Sain, B.; Reineke, B.; Zhao, R.; Meier, C.; Huang, L.; Jiang, Y.; Zentgraf, T. Nonlinear Wavefront Control by Geometric-Phase Dielectric Metasurfaces: Influence of Mode Field and Rotational Symmetry. *Adv. Opt. Mater.* **2020**, *8*, 1902050.

(23) Dasgupta, A.; Gao, J.; Yang, X. Atomically Thin Nonlinear Transition Metal Dichalcogenide Holograms. *Nano Lett.* **2019**, *19*, 6511−6516.

(24) Löchner, F. J. F.; Mupparapu, R.; Steinert, M.; George, A.; Tang, Z.; Turchanin, A.; Pertsch, T.; Staude, I.; Setzpfandt, F. Controlling second-harmonic diffraction by nano-patterning MoS$_2$ monolayers. *Opt. Express* **2019**, *27*, 35475−35484.

(25) Autere, A.; Jussila, H.; Dai, Y.; Wang, Y.; Lipsanen, H.; Sun, Z. Nonlinear Optics: Nonlinear Optics with 2D Layered Materials. *Adv. Mater.* **2018**, *30*, 1870172.

(26) Seyler, K. L.; Schaibley, J. R.; Gong, P.; Rivera, P.; Jones, A. M.; Wu, S.; Yan, J.; Mandrus, D. G.; Yao, W.; Xu, X. Electrical control of second-harmonic generation in a WSe$_2$ monolayer transistor. *Nat. Nanotechnol.* **2015**, *10*, 407−411.

(27) Zeng, H.; Dai, J.; Yao, W.; Xiao, D.; Cui, X. Valley polarization in MoS$_2$ monolayers by optical pumping. *Nat. Nanotechnol.* **2012**, *7*, 490−493.

(28) Mak, K. F.; He, K.; Shan, J.; Heinz, T. F. Control of valley polarization in monolayer MoS$_2$ by optical helicity. *Nat. Nanotechnol.* **2012**, *7*, 494−498.

(29) Xiao, J.; Ye, Z.; Wang, Y.; Zhu, H.; Wang, Y.; Zhang, X. Nonlinear optical selection rule based on valley-exciton locking in monolayer WS$_2$. *Light: Sci. Appl.* **2015**, *4*, e366−e366.

(30) Dasgupta, A.; Gao, J.; Yang, X. Second-harmonic optical vortex conversion from WS$_2$ monolayer. *Sci. Rep.* **2019**, *9*, 8780.

(31) Jones, P. H.; Maragò, O. M.; Volpe, G. *Optical Tweezers: Principles and Applications*; Cambridge University Press: 2015.

(32) Yin, X.; Ye, Z.; Chenet, D. A.; Ye, Y.; O'Brien, K.; Hone, J. C.; Zhang, X. Edge Nonlinear Optics on a MoS$_2$; Atomic Monolayer. *Science* **2014**, *344*, 488.

(33) Chen, J.; Wang, K.; Long, H.; Han, X.; Hu, H.; Liu, W.; Wang, B.; Lu, P. Tungsten Disulfide−Gold Nanohole Hybrid Metasurfaces for Nonlinear Metalenses in the Visible Region. *Nano Lett.* **2018**, *18*, 1344−1350.

(34) Shi, J.; Liang, W.-Y.; Raja, S. S.; Sang, Y.; Zhang, X.-Q.; Chen, C.-A.; Wang, Y.; Yang, X.; Lee, Y.-H.; Ahn, H.; Gwo, S. Plasmonic Enhancement and Manipulation of Optical Nonlinearity in Mono-layer Tungsten Disulfide. *Laser Photonics Rev.* **2018**, *12*, 1800188.